

International Journal of Multidisciplinary Research and Growth Evaluation.



AI-Enhanced Motion Tracking for Obesity Physiotherapy: A Wireless Sensor-Based Approach

VV Manjula Kumari

CEO and Senior Consultant for Obesity, Varanaa's Health Care Research and Training Organization, India

* Corresponding Author: VV Manjula Kumari

Article Info

ISSN (online): 2582-7138

Volume: 05 Issue: 04

July - August 2024 Received: 08-04-2024 Accepted: 10-05-2024 Page No: 1410-1420

Abstract

Obesity-related mobility issues often require structured physiotherapy interventions to enhance movement efficiency, posture, and functional rehabilitation. However, access to real-time exercise feedback is limited in traditional settings. This paper presents an AI-powered motion tracking system that supports obesity physiotherapy treatments by providing wireless movement analysis, posture correction, and real-time rehabilitation feedback. The system integrates an Inertial Measurement Unit (IMU)-based motion sensor node with wireless data transmission and real-time monitoring to assist obesityfocused physiotherapy exercises. The device provides continuous feedback on movement accuracy, ensuring proper form during low-impact exercises designed for overweight patients. With an autonomy of 28 hours and wireless data analysis capabilities, this technology offers a cost-effective physiotherapy monitoring solution for both clinical and home-based obesity rehabilitation programs. Experimental results demonstrate that the sensor achieves high accuracy (error margin of $\pm 3^{\circ}$) in motion tracking, making it a viable tool for personalized weight-loss physiotherapy interventions. This research highlights the importance of Aldriven motion tracking in enhancing physiotherapy outcomes for obesity treatment.

DOI: https://doi.org/10.54660/.IJMRGE.2024.5.4.1410-1420

Keywords: Physiotherapy, E-Health, Motion Sensing, Wireless Charging, Wireless Connectivity, and Low Power

1. Introduction

Context: Evolution of Physiotherapy. In recent decades, physiotherapy has evolved significantly beyond conventional stretching and massage practices. Today, it encompasses a wide spectrum of applications, including rehabilitation following surgery, managing neurological disorders, and preventing occupational injuries. This transformation has been driven by advancements in medical technology, particularly in diagnostic imaging, which has enabled more precise identification of injuries. As a result, physiotherapists can now develop personalized treatment plans with improved accuracy ^[1]. This study explores the integration of technology at the patient level to enhance both rehabilitation and preventative physiotherapy techniques.

Focus: Motion-Sensing Technology. This paper presents an inertial measurement unit (IMU)-based sensor system de-signed to monitor and visualize patient movements during both therapeutic exercises and daily routines. The key design priorities for this system include energy efficiency, simplicity, affordability, and compactness. The final prototype has a maximum diameter of 6 cm, a weight of less than 50 g, and an estimated production cost of approximately 30 C, with the potential for further cost reductions through mass production. Due to its medical application, the device is hermetically sealed, necessitating a wireless charging mechanism. Moreover, real-time sensor data is wirelessly transmitted to a base station for further analysis. An integrated calibration process enhances measurement precision compared to uncalibrated devices.

Enhancements Over Existing Solutions. Unlike existing alternatives [2, 3], the proposed sensor prioritizes raw data acquisition rather than automated processing. However, it allows for a meaningful graphical representation of the collected data for ease of interpretation. A key distinguishing feature of this design is its focus on accessibility and usability for both physiotherapists and patients.

By maintaining a low-complexity, cost-effective approach, the proposed motion sensor system delivers functionality comparable to current solutions but at a significantly lower cost. Although smartwatches are widely used for activity tracking, they are not optimized for precise physiotherapy monitoring as they are not designed for placement on different parts of the body. Furthermore, they do not meet the affordability and simplicity criteria central to the proposed system.

Contribution. This study introduces a novel sensor system that combines cost-effective components with a contactless operation, featuring an automated calibration process specifically designed for e-treatment applications in physiotherapy. The contributions of this research are threefold. First, the design and implementation of a wireless sensor module that integrates wireless communication and charging while meeting the established constraints. The open-source design is accessible on GitHub [4]. Second, an efficient and straightforward single-step calibration method has been proposed, enhancing usability and system dependability. Lastly, the sensor through photogrammetry has been validated showcasing its practical feasibility with affordable and easily accessible equipment in real-world conditions. Additionally, this paper provides relevant context regarding technological advancements and potential applications.

Paper Structure. The structure of this paper is as follows: Section 2 details the design principles of the wireless sensor module, addressing aspects such as calibration, wireless connectivity, and power efficiency. The prototype, which aligns with the initial design goals, is also introduced. Section 3 evaluates the sensor's accuracy and functionality, employing cost-effective tools instead of highend laboratory instruments. Beyond static validation, Section 4 examines the sensor's dynamic performance, particularly in motion-based physiotherapy applications. Section 5 discusses the real-world applicability of this wireless sensor in e-treatment scenarios and explores possible enhancements. Finally, Section 6 provides a summary of the key insights and outlines directions for future research.

2. Streamlined design of a wireless motion sensor node The development of the sensor node was governed by several fundamental design criteria:

- Precision: The device must reliably capture human motion. With proper calibration, an accuracy level of ±2° is attainable, sustaining a sampling rate of 50 Hz ^[5].
- Ease of Use: The system should be intuitive and accessible to individuals with no technical or medical background. To improve usability, I incorporated wireless charging for effortless maintenance. Furthermore, the data transmission is entirely wireless, eliminating cumbersome cables and ensuring unrestricted mobility.
- Operational Autonomy: The device should allow users to concentrate on its application rather than frequent recharging. Thus, a minimum operational time of 5 hours and a maximum recharge duration of 1.5 hours were established as essential requirements.
- Cost-Effectiveness: For broader accessibility across various applications, the device must remain affordable, ensuring its usability for both professional and individual users.

At the core of the sensor node is an Inertial Measurement Unit (IMU), enabling wireless data transfer to a receiver while supporting wireless charging. Figure 1 illustrates the system architecture. The primary specifications and functionalities of the sensor node are elaborated on below.

A. Sensors

Motion tracking can be achieved using various methods. One commonly used approach is a vision-based motion capture system ^[6], which provides high accuracy but is costly and has limitations regarding adaptability to different environments. A more practical alternative is motion tracking using an Inertial Measurement Unit (IMU).

An IMU integrates multiple onboard sensors, with 6-DoF configurations being widely employed in recent research $^{[7,\,8]}.$ However, these systems suffer from cumulative drift errors that cannot be corrected over time. To address this, a 9-DoF IMU is utilized, incorporating an additional magnetometer to provide an absolute reference. The selected IMU (ICM-20948 from Invensense) $^{[9]}$ was chosen for its low power consumption and high accuracy. The gyroscope operates within a ± 2000 degrees per second (dps) range, the accelerometer is set at ± 4 G, and the magnetometer supports a maximum field strength of $\pm 4900~\mu T$. The sampling rate for all sensors is fixed at 50 Hz.

Sensor fusion techniques are essential to achieve accurate orientation estimation. A Digital Motion Processor (DMP), as implemented in [10], can efficiently handle complex sensor fusion algorithms while offloading computational demands from the main processor, leading to better energy efficiency. However, relying on proprietary sensor fusion techniques restricts flexibility and control over sensor calibration. By implementing custom sensor fusion algorithms, I maintain full control over the process, enabling optimization tailored to specific application needs.

Certain systems utilize Kalman filters for sensor fusion [7], achieving precise estimations at the expense of computational intensity. On the other hand, complementary filters—though computationally efficient—often provide less accuracy. This approach integrates a high-pass filter for gyroscope data with a low-pass filter for accelerometer readings. However, during prolonged dynamic motion, its reliability diminishes. Prior research such as [8] applies complementary filters for static angle estimations, heavily depending on accelerometer measurements. Given the necessity of maintaining high accuracy during movement while keeping computational demands low, I opted for the Madgwick filter [11], which effectively balances these constraints. The algorithm is deployed on the primary microcontroller (ARM Cortex M0+ microcontroller, EFM32HG from Silabs) [12] utilizing quaternion-based computations for orientation estimation.

$$p = w + x \cdot i + y \cdot j + z \cdot k \tag{1}$$

Quaternions provide a robust framework for representing orientation, circumventing the gimbal lock issue commonly encountered in Euler angles—where, at a pitch of 90°, roll and yaw become indistinguishable. Furthermore, orientation estimation proves unreliable at extreme angles $^{[13]}.$ The efficiency of the Madgwick filter enables its execution at low processing speeds while maintaining accuracy. Under the 50 Hz sampling rate utilized in the sensor module, the static error is confined to $\pm 1^\circ$ while the dynamic error remains within $\pm 2^\circ$ $^{[11]}$

Fig 1: System architecture: The sensor module integrates an Inertial Measurement Unit (IMU), wireless charging functionality, and data transmission capabilities to a receiver unit.

To extend battery longevity, the sensor module remains in a low-power state whenever feasible. Upon detecting movement, an always-active accelerometer triggers an interrupt signal to activate the system. This sequence is depicted in Figure 3.

Upon activation, the gyroscope lacks an initial orientation reference, necessitating roughly 30 seconds to stabilize. The degree of initial orientation error is influenced by the difference between the sensor's orientation at power-up and

its final recorded state before entering sleep mode. To expedite the stabilization process, the parameters of the Madgwick filter are dynamically adjusted, initially prioritizing accelerometer and magnetometer data. As the system establishes a stable orientation reference, it transitions into a high-accuracy mode, where gyroscope data primarily dictates orientation, while accelerometer and magnetometer readings serve as minor corrective inputs.

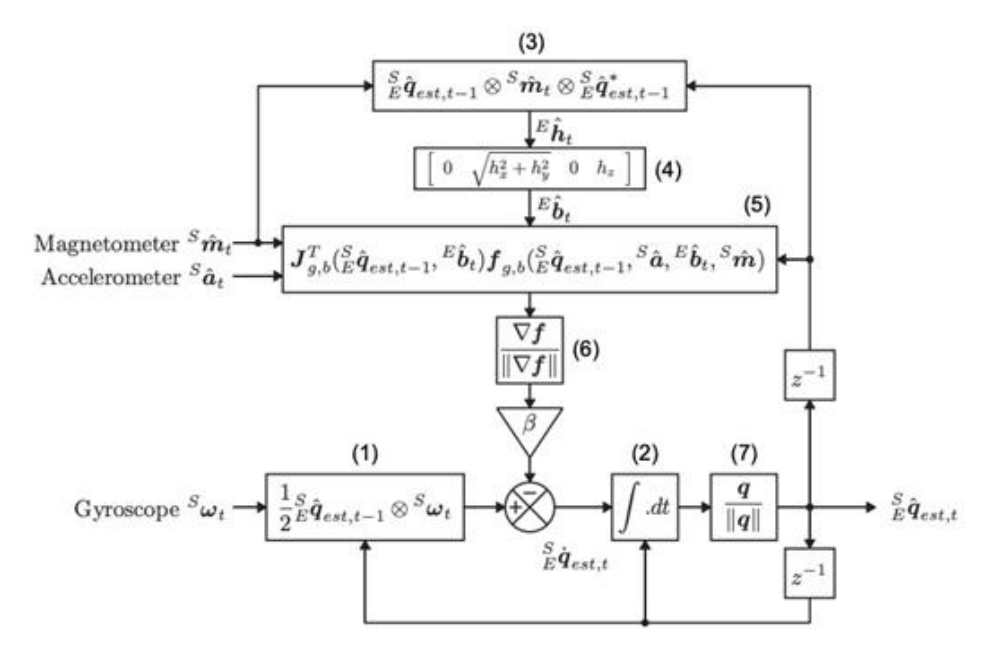


Fig 2: Illustrative block diagram of the Madgwick orientation estimation method [11].

An inactivity detection mechanism is integrated to optimize power consumption. The gyroscope values are periodically assessed every second via an interrupt-driven routine controlled by a Real-Time Counter (RTC). If no significant movement is detected, the system automatically shifts into a low-power sleep state, reducing energy expenditure.

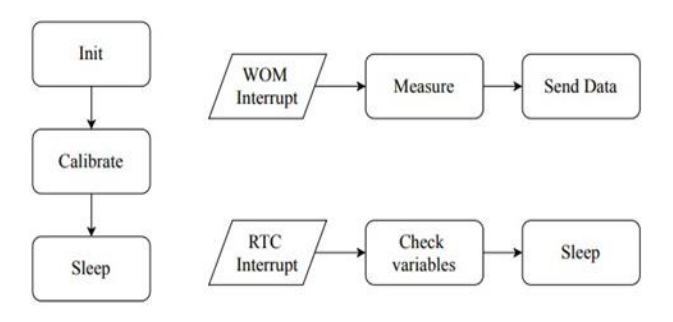


Fig 3: Process flow of sleep mode engagement and reactivation. The system remains in low-energy mode until motion is detected, prompting a switch to active operation.

B. Calibration

Calibration is fundamental in motion-tracking systems, substantially improving measurement precision. This system employs a single manual calibration process, striking a balance between energy efficiency and high accuracy by utilizing a low-power microcontroller. Initially, the gyroscope and accelerometer undergo calibration by positioning the sensor unit on a stable, leveled surface. Under these conditions, the gyroscope should register zero angular velocity, while the accelerometer should experience only gravitational acceleration, free from additional external forces.

To ensure high precision, the accelerometer and gyroscope are initially set to their most sensitive measurement configurations of ± 250 dps and ± 2 G full scale, respectively. A large volume of data is acquired by utilizing the First In First Out (FIFO) buffer of the Inertial Measurement Unit (IMU). From these collected measurements, the bias offsets of both sensors are computed and later removed from all subsequent readings. Following this calibration process, the measurement ranges are reset to ± 2000 dps and ± 4 G full

scale.

Calibration of the magnetometer is performed by rotating the sensor a full 360° along each of its three axes or by executing a figure-eight motion. During this procedure, the sampling rate is temporarily increased to 100 Hz to maximize data acquisition and enhance calibration accuracy. After the process is completed, the magnetometer sample rate is reverted to 50 Hz. Figure 4 illustrates a 2D projection of the three intersecting planes of the 3D sphere generated by the sensor's movement.

IMU readings can be affected by two principal distortions: hard iron and soft iron effects ^[14]. Hard iron distortions arise due to the presence of permanent magnetic materials, resulting in a consistent offset in the observed magnetic sphere. These offsets are determined by locating the center of the sphere and subtracting this value from subsequent measurements. Soft iron distortions, conversely, originate from materials such as iron, which do not generate magnetic fields but distort the surrounding magnetic environment. This type of distortion typically manifests as elliptical rather than circular patterns in 2D plots.

To correct soft iron distortions, a scaling factor is applied to each axis. The calibration process involves determining the minimum and maximum compass readings along each axis. Using these values, the span of readings for all three axes is computed, followed by the mean span across the axes. The scale factor for each axis is then obtained by dividing the mean span by the individual axis span, as shown in Equation

$$SF_{x} = \frac{\max(B_{x}) - \min(B_{x}) + \max(B_{y}) - \min(B_{y})}{3 \cdot (\max(B_{x}) - \min(B_{x}))} + \frac{\max(B_{z}) - \min(B_{z})}{3 \cdot (\max(B_{x}) - \min(B_{x}))}$$
(2)

A sample calculation for the x-axis scale factor is illustrated below:

After implementing these corrections, the three circles appear uniformly round and centered, as depicted in Figure 5, verifying the accuracy of the calibration method.

C. Wireless Connectivity

Numerous wireless communication standards are available for Wireless Body Area Networks (WBANs). In this section, I briefly discuss the most relevant options for the proposed system.

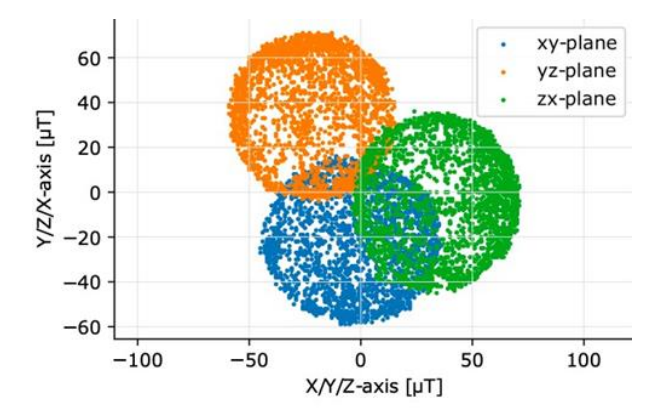


Fig 4: 2D visualization of a sphere when the sensor node is rotated around each axis before applying calibration. The deformation of the circles into ellipses (indicating a distorted sphere in 3D) is a result of soft iron interference. Additionally, hard iron distortions cause the circles' centers to be offset from the origin.

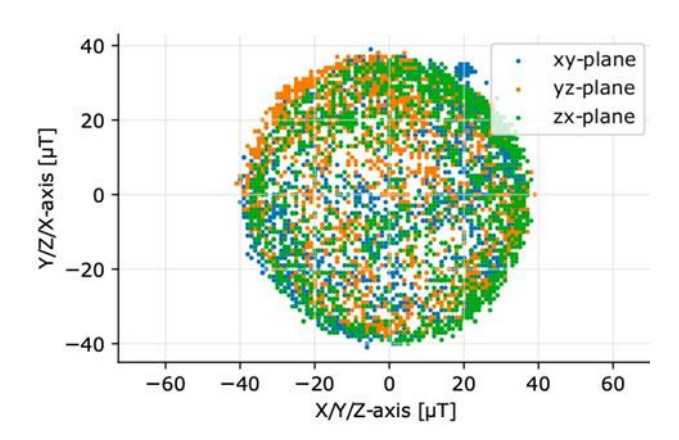


Fig 5: 2D visualization of a sphere when the sensor node is rotated around each axis after calibration. The circles now appear perfectly round (indicating an almost ideal sphere in 3D), and no displacement between the circles' centers and the origin is observed.

ZigBee, a low-power communication standard, is built on the IEEE 802.14.4 protocol. It allows communication over distances of up to 100 meters and supports a mesh topology. However, its relatively low data transfer speed, reaching a maximum of 250 kbps at 2.4 GHz, makes it less suitable for this application [15]. Another alternative is Z-Wave, which provides data rates between 40 kbps and 100 kbps and can communicate over a range of 30 meters. Since ZWave operates in the 900 MHz frequency band, it avoids interference from common 2.4 GHz signals such as WiFi. This characteristic makes it widely used in energy-efficient sensor networks, particularly in home automation. However, its master-slave topology results in a communication delay of approximately 200 ms [16].

Bluetooth, which follows the IEEE 802.15.1 standard, offers significantly higher data rates of up to 2 Mbps and a range extending to 100 meters. It is widely used for transmitting both data and audio, utilizing a master-slave communication model ^[17]. In this design, Bluetooth Low Energy (BLE) is the most suitable option due to its optimized power consumption. BLE supports a peak data rate of 1 Mbps and operates in either a star topology or a mesh network ^[16]. A key benefit of BLE is its seamless integration with smartphones and Bluetoothenabled devices, eliminating the requirement for an external receiver.

Table 1: Evaluation of wireless communication technologies: zigbee, z-wave, bluetooth 5, ble, and wifi (???).

Technology	ZigBee	Z- Wave	Bluetooth 5	BLE	WiFi
Maximum Power Consumption	100 mW	1 mW	100 mW	10 mW	>100 mW
Maximum Coverage Range	100 m	30 m	100 m	<100 m	1000 m
Peak Data Rate	250 kbps	100 kbps	2 Mbps	1 Mbps	54 Mbps
Cost Factor	Low	High	Very Low	Very Low	Average

WiFi, based on the IEEE 802.11 standard, delivers a notably higher data transmission rate of 54 Mbps. Despite this advantage, its substantial energy consumption renders it impractical for power-sensitive applications [17]. Furthermore, alternative proprietary approaches have been evaluated, demonstrating potential power savings through

optimized packet structuring. Table I provides an overview of various wireless connectivity solutions, comparing their power consumption, coverage, speed, and cost. BLE emerges as the preferred choice due to its optimal balance of power efficiency, range, transmission rate, affordability, and interoperability.

For seamless data communication, a Wireless Body Area Network (WBAN) is designed utilizing BLE, given its low power draw, high data throughput, and broad compatibility [16]. The selected BLE module, Proteus II (AMB2623 module from WE, based on the nRF52832) [17], was chosen for its compact dimensions and integrated PCB antenna. Data transmission occurs at zero dBm. The transmitted packet, sent at a frequency of 50 Hz, consists of a header, receiver module ID, received signal strength indicator (RSSI), sensor output, and a checksum for error validation. The packet structure is depicted in Figure 6.

			face				2.2.0.00	ule ID			RSSI		A	ta x				ta y			Dat			200 011 0	Checksum
0:	2	84	0B	00	BC	04	20	DA	18	00	XX	x	x	x	x	у	у	у	у	z	z	z	·z	%	CS

Fig 6: Structure of a Bluetooth Low Energy (BLE) data packet: The packet consists of a preamble, a device identifier, three orientation angles, the battery level (as a percentage), and an error-checking code.

The quaternion values generated by the Madgwick sensor fusion algorithm are transformed into Euler angle representations and stored as floating-point numbers. Each of these floats occupies four bytes in memory [19], ensuring retention throughout data transmission. Additionally, a single byte is allocated to represent the battery level. To optimize power consumption, the embedded software implements a lowpower mode that activates if no connection is established within five seconds. The system is also designed with an automatic reconnection functionality. On the receiving end, an STM32L4+ microcontroller is utilized, integrated into an ST NUCLEO L45ZI development platform $^{[20]}$, and paired with an identical BLE module. The reception process employs an interrupt-based mechanism coupled with a circular buffer [21]. Data handling occurs asynchronously, after which a secondary UART interface forwards the received data to a computer for further processing. A threedimensional visualization of the orientation data is rendered using VPython.

D. Wireless Charging

Inductive wireless energy transfer is widely employed for charging batteries in smartphones, wearables, and Internet of Things (IoT) devices. To ensure secure and efficient energy transfer, various implementation standards have been established, including Qi, PMA, and AirFuel. For low-power applications—typically under 5 W—proprietary solutions like Semtech's "LinkCharge Low Power" technology are often utilized. Common use cases for this technology include wearable electronics, electric toothbrushes, sensors, and LoRa-based sensor networks [22]. Companies such as ST Microelectronics also offer wireless power solutions tailored for smartwatches and battery-operated IoT devices. Another alternative is designing a custom Wireless Power Transfer (WPT) system instead of relying on existing standards. However, developing a more effective system is challenging due to the extensive research already conducted in the 5 W WPT space.

Among the available standards, Qi has emerged as the most widely adopted in recent years. The Wireless Power Consortium (WPC) oversees its development and standardization. Moreover, PMA, AirFuel, and WPC have initiated joint efforts to improve compatibility. Devices certified under the Qi protocol can communicate with one another, enabling seamless interoperability between Qienabled devices and chargers. The standard incorporates multiple safety features, such as foreign object detection, overvoltage AC clamp protection, and thermal shutdown

mechanisms to ensure a reliable charging process ^[23]. Earlier generations of wirelessly rechargeable smartwatches relied on proprietary WPT protocols. However, modern wearable devices have largely transitioned to the Qi standard. Conversely, smartphones that support wireless charging have implemented Qi from the outset. Many contemporary smartphones are also equipped with "Reverse Charging," a functionality that enables their internal coil to wirelessly power other Qi-compatible devices ^[24]. This feature allows users to charge their smartwatches directly from their smartphones, making Qi an ideal choice for sensor modules. Given that Qi chargers and reverse-charging smartphones are already prevalent in households, users can conveniently recharge sensor modules within their homes.

This study delves deeper into the practical implementation of the battery charging circuit within the sensor node architecture. Since the energy transfer is based on the Qi protocol, a Qi-compliant receiver integrated circuit (IC) was selected for integration. The Texas Instruments Qi receiver IC (BQ51050) (23) was chosen due to its high efficiency, wireless power reception capability, built-in rectification, and integrated battery charging features. Specifically, the BQ51050A variant was selected for its compatibility with Li-Ion batteries and its predefined 4.20 V output voltage limit. Additionally, an inductor coil (I 760308101214) [25] was chosen due to its compact design and high Q-factor. The charging current is regulated at 200 mA, while a termination current of 20 mA is maintained to ensure a fast yet safe charging process. To further enhance operational safety, a Negative Temperature Coefficient (NTC) resistor is incorporated for temperature control, triggering an automatic cut-off mechanism when the temperature reaches 60°C. Given the compact size of the coil, additional shielding was implemented to optimize the performance of the Wireless Power Transfer (WPT) system.

Figure 7 illustrates the two primary coils within the system alongside their corresponding resonant circuits. Each charging module incorporates a power transmitter coil, while every battery-operated device contains a receiver coil. The efficiency of the wireless charging process is greatly enhanced through the implementation of LC resonant circuits on both the transmitting and receiving sides. Since the coupling coefficient between the coils is relatively low, the inclusion of a resonant circuit helps mitigate leakage inductance and boosts overall performance (26). A Qi

charging station consists of an amplifier connected to an LC series resonant circuit. On the receiving side, the LC resonance network is comprised of elements Lr, Ca1, and Ca2. The necessary capacitance values are determined using the equations given below:

$$C_p = \frac{1}{(2\pi f_p)^2 L_t}$$
 (3)

$$C_q = \left((f_q 2\pi)^2 L_r - \frac{1}{C_p} \right)^{-1} \tag{4}$$

Here, Lt refers to the measured inductance when the receiver coil is positioned on the charging station, while Lr signifies the inductance measured in free space. The parameters fp and fq are set at 100 kHz and 1 MHz, respectively [23].

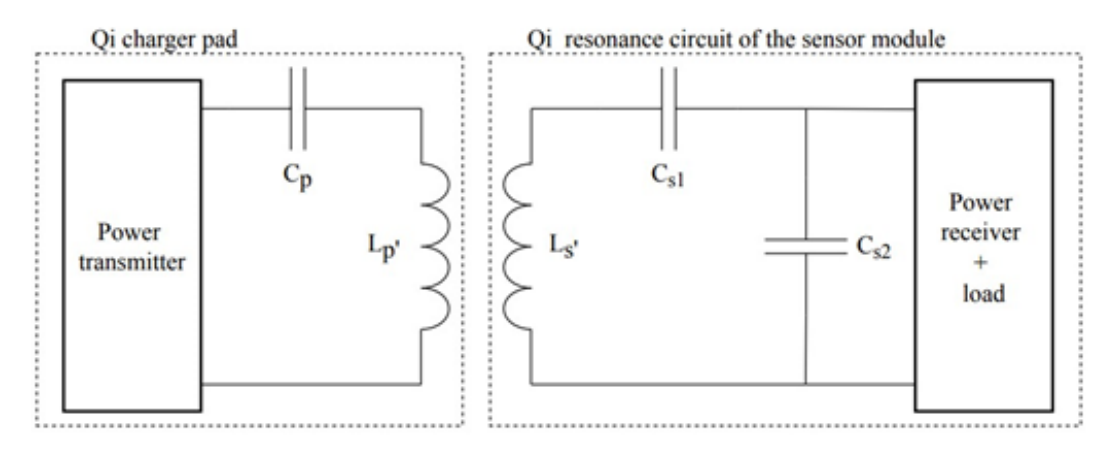


Fig 7: Wireless energy transfer configuration. A Qi power transmitter connected to a Qi receiver and load, employing LC resonance.

By substituting the computed values and selecting commercially available circuit components, the capacitance values determined for Cb1 and Cb2 are 100 nF and 1 nF, respectively. Furthermore, three additional capacitor types play a vital role in the system: the BOOT, COMM, and CLAMP capacitors. The BOOT capacitor functions as a bootstrap capacitor, which is crucial for enabling the high-side MOSFETs within the synchronous rectifier.

Meanwhile, COMM capacitors enable communication with the charging station through capacitive load modulation. This technique introduces an extra capacitive element into the resonance circuit, altering its resonant frequency. The charging pad detects this frequency deviation, allowing seamless communication between the receiver's charging module and the transmitter system. The standard values for resistive load modulation are obtained from the datasheet.

Additionally, CLAMP capacitors are instrumental in overvoltage protection by reacting to rectified voltages surpassing 15 V. This reaction adjusts the resonance frequency to prevent excessive voltage buildup in the circuit. According to the datasheet recommendations, the selected capacitance values for the BOOT, CLAMP, and COMM capacitors are 10 nF, 470 nF, and 47 nF, respectively [13].

E. Optimization for Low Energy

A key aim of this research is to design a sensor node with optimal energy efficiency. A lithium-ion battery has been selected due to its high energy density and lightweight nature. The battery chosen for this prototype is a cylindrical cell with a 200 mAh capacity and supports recharging. To improve ease of use and compatibility, Qi-standard wireless charging has been integrated. The system operates at a regulated voltage of 2V, managed by an ultra-low quiescent current (Iq) buck converter. In comparison to a low-dropout (LDO) regulator, a buck converter ensures significantly higher efficiency, even when the system is in standby mode.

The inertial measurement unit (IMU) functions at a voltage level of 1.8V. Given the minimal voltage drop of 0.2V,

employing an LDO is the more energy-efficient approach. By setting the system voltage at 2V instead of the standard 3.3V, a theoretical reduction in power consumption of approximately 9.610 mW is achieved when quiescent currents are disregarded. This leads to an estimated improvement of 29.3% in overall battery autonomy. The sensor node consumes 0.102 mW in sleep mode and 25.839 mW during active measurement operations. As a result, the system can function continuously for 28 hours before requiring a recharge, while in sleep mode, it can last up to 261 days—surpassing the initially estimated five-hour operational limit.

With an active power usage of 25.839 mW, the system achieves exceptionally low energy consumption for its category, leaving little room for additional improvements, given the current hardware setup. However, the sleep-mode power draw of 0.102 mW could be further optimized by fully disconnecting the Qi wireless charging module when not in operation. This would eliminate quiescent current losses, which can be realized by integrating a MOSFET switch.

F. Prototype

A well-designed, compact structure is crucial for effortless placement on the body. The sensor module features a circular design with smooth contours to maximize user comfort. The final prototype weighs 38 g and has dimensions of $6 \text{ cm} \times 1.5 \text{ cm}$. Figure 8 illustrates the structural layout of the casing.

- The wireless charging coil is positioned at the base,
- Secured within the housing through integrated supports,
- The power source is placed directly above the coil,
- Followed by the printed circuit board (PCB), ^[5] stabilized by four structural pins inside the enclosure, ^[6] The entire assembly is enclosed using a twist-lock cover.

For initial testing, the casing has not been fully sealed. However, enhanced water resistance can be achieved by applying a sealing compound to the twist-lock mechanism. Figure 9 showcases the fully assembled sensor module. The

overall cost of the components, including the case, amounts to 28C, which ris reduced to 22C when excluding the enclosure.

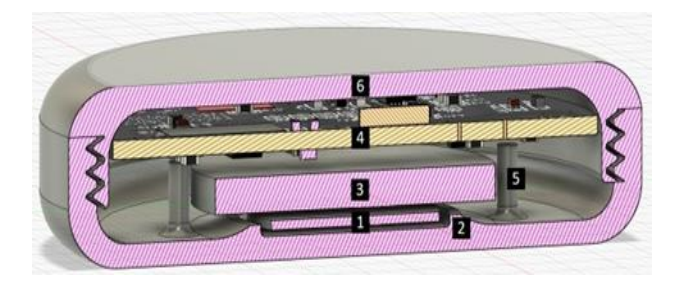


Fig 8: Cross-sectional representation of the sensor module. 1: wireless charging coil, 2: support structures, 3: battery, 4: PCB, 5: structural pins, 6: locking cover.



Fig 9: Assembled sensor module in a 3D-printed casing. (a) Bottom view: wireless charging coil and battery. (b) Top view: IMU, microcontroller, and BLE module.

3. Validation with commonly available tools

High-precision equipment is typically employed to validate motion data collected from the sensor module. The static calibration of the IMU was previously performed using a computer-controlled pan-tilt platform to position the sensor at predefined angles or by utilizing a Vicon motion capture system (6; 8; 27). Similarly, when evaluating the Madgwick filter, the Vicon system was employed for validation [28]. Despite delivering high accuracy, these tools are often expensive, difficult to access, and require extensive setup time.

To provide a more practical and cost-effective validation approach, an alternative method leveraging widely available tools is proposed. Photogrammetry serves as an effective technique to assess the sensor module's accuracy. This method involves capturing sequential images to analyze the sensor's positional data. By comparing IMU-derived measurements with those extracted from photographic analysis, static error quantification is possible. This validation strategy is advantageous as it enables assessments using consumer-grade equipment across diverse environments.

Consumer-grade cameras, such as those integrated into smartphones, frequently introduce distortions due to lens imperfections and suboptimal image resolution. To counteract these challenges, the camera is mounted in a horizontal orientation and aligned perpendicularly to the surface, effectively removing foreshortening artifacts. Moreover, the sensor is centrally positioned within the captured frame, minimizing radial distortions. This configuration eliminates the requirement for explicit camera calibration. To further enhance accuracy, strategically placed markers are used, as demonstrated in Figure 10, ensuring their relative positions are measured with a precision of ± 2 mm.



Fig 10: Sensor validation methodology leveraging photogrammetry with readily available commercial equipment. By correlating IMU data with image derived measurements, static error estimation is possible for both pitch and roll angles.

Since the primary focus is on angular measurements, the acquired images are mapped onto the sensor node's reference frame. To enhance measurement accuracy, a lever is affixed to the sensor unit. The sensor's angle is determined by identifying the lever's endpoints (highlighted by red and green markers in Figure 10) and mapping them to a reference coordinate system, established by the surrounding markers. By comparing the IMU-derived values with those extracted from the images, the static error in pitch and roll measurements can be quantified. While this study emphasizes static measurements, dynamic assessments are feasible by capturing video sequences instead of single images and synchronizing video frames with the sensor's output. This technique enables angular determination at the frame level. Manual annotation of key points in each frame be replaced with automated image-tracking methodologies [29, 30].

Table 2 presents the measurement results. To verify roll and pitch angles, the experimental setup depicted in Figure 10 is employed, with the sensor rotated by 90° between measurements. Since yaw lacks an absolute reference frame, relative measurements are obtained using the setup in Figure 11, where the sensor and markers are placed on a horizontal plane instead of a vertical surface. Multiple static measurements were conducted, revealing that the sensor experiences a drift of 2° over a 30-minute period. The recorded mean error values are 3.06° for pitch, 2.75° for roll, and 4.04° for yaw.

Table 2: Results of static pitch, roll, and yaw angle measurements with corresponding errors at various angles.

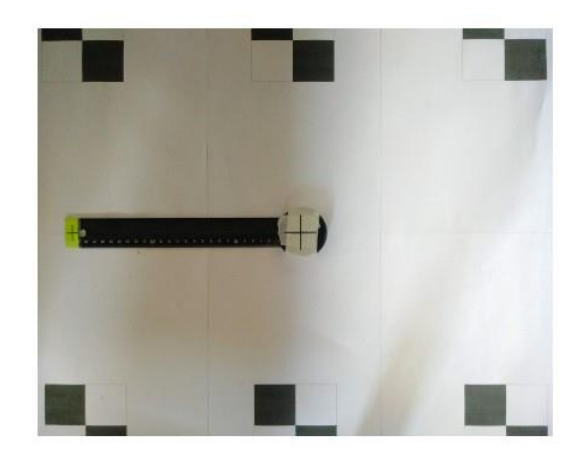
Target Angle [°]	Reference [°]	Sensor [°]	Error [°]
	Pitch		
0	0.08	-3.2	3.28
45	44.76	42.5	2.26
90	90.19	95.04	-4.85
180	178.45	176.6	1.85
	Roll		
0	0.47	1.8	-1.33
45	48.41	44.8	3.61
90	90.15	87	3.15
180	180.01	177.1	2.91
	Yaw		
45	48.03	45.1	2.93
90	95.49	88.9	6.59
180	182.18	185.2	-3.02
270	274.12	270.5	3.62

A possible alternative approach involves simultaneously capturing roll, pitch, and yaw angles using a stereo or multicamera setup to acquire 3D representations of the lever's endpoints. However, this method introduces additional complexities, including the need for calibration and synchronization, as well as reduced depth measurement accuracy. Some inconsistencies were noted in the recorded measurements. Specifically, the yaw orientation at 90° displayed irregularities, most likely due to interference from nearby magnetic objects. Electronic devices such as mobile phones and speakers generate magnetic fields that can disrupt sensor readings, as these interferences fluctuate relative to the sensor's frame of reference and thus cannot be fully mitigated through calibration. To enhance measurement reliability,

users should maintain a minimum separation of 0.5 meters from such sources. Additionally, the pitch deviation at 90° was observed to be substantial, which is attributed to the inherent limitations of Euler angle representation near this orientation [13].

4. Empirical Validation Through Physical Exercises

To further evaluate the sensor module's dynamic characteristics and real-world usability, two movement-based assessments were conducted. The first exercise required a participant to kneel while placing their hands on the ground and alternately curve and arch their back, highlighting the spine's cyclic concavity. This process is depicted in Figure 12. oscillation of ± 45



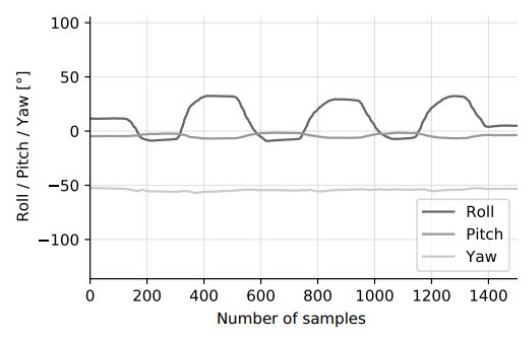


Fig. 13. Analysis of rounded-back and hollow-back motion. A periodic

Fig 11: Validation of yaw axis measurements using a photogrammetry-based approach.

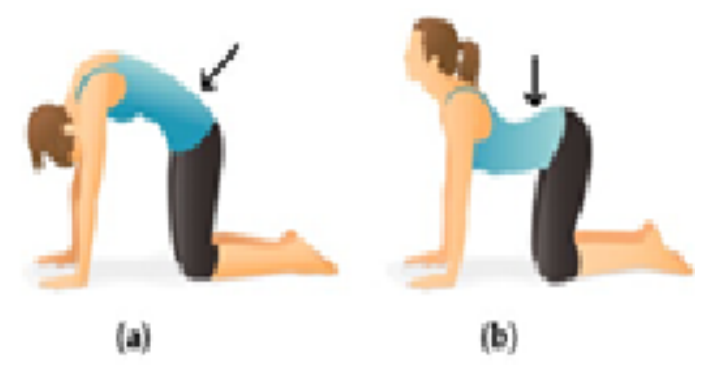


Fig 12: Depiction of the initial exercise: cyclical concavity of the spine (Images sourced from Pocket Yoga (www.pocketyoga.com)). The sensor placement is denoted by arrows. (a) Initial posture. (b) Final posture.

The respective measurement results are visualized in Figure 13. The exercise was repeated three times, and the roll axis data exhibited a periodic oscillation with an angular range of approximately $\pm 45^{\circ}$. Meanwhile, the pitch axis data showed minor lateral tilts in the lower back, whereas the yaw axis maintained stability, as anticipated.

A second assessment analyzed the rotational motion of the torso, as illustrated in Figure 14. During this exercise, the participant performed lateral trunk rotations while ensuring the stability of the lower body. The results, captured in Figure 15, indicated an angular displacement of around $\pm 50^{\circ}$ along the yaw axis. Additionally, slight deviations in roll and pitch values were detected. These experiments serve as an initial verification of the sensor's dynamic behavior. The acquired dataset suggests that the current sampling rate suffices for obtaining reliable measurements. However, further validation using high-precision photogrammetry or dedicated

motiontracking systems is required for definitive accuracy verification remain largely stable.

5. Potential Applications In Digital Rehabilitation And Future Enhancements

This section explores the integration of compact, costeffective, and user-friendly sensor modules in physiotherapy applications. A comparative analysis with existing solutions is conducted, and possible system enhancements are discussed to introduce advanced functionalities beneficial for both personal and clinical use.

A. Potential of e-Treatment in Physiotherapy

The proposed wireless sensor node has been specifically developed to meet the demands of physiotherapy by providing technological assistance for both treatment and prevention. This innovation enables what I term as e-

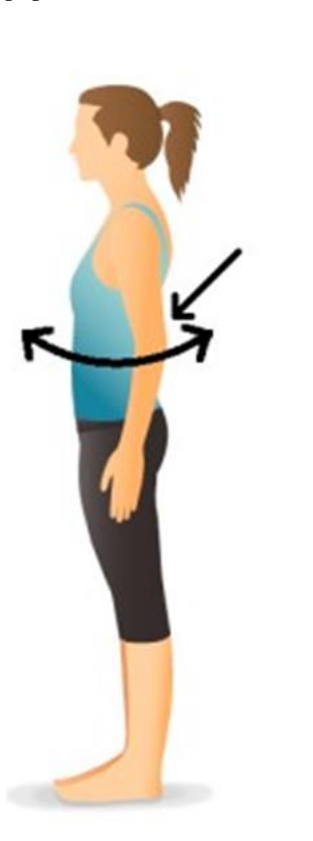
treatment, a form of remote physiotherapy supported by realtime wireless sensor measurements.

From a therapeutic perspective, patients can utilize this sensor to aid physiotherapists in tracking and assessing their rehabilitation progress, even when performing exercises independently at home. In the realm of preventive healthcare, the sensor allows continuous monitoring of movement patterns and flexibility evaluations. Workplace monitoring is particularly valuable, as repetitive strain and improper postures are major contributors to neuromusculoskeletal conditions [31].

A fundamental advantage of e-treatment lies in its ability to be conducted remotely. In this framework, the patient does not need to be physically present in a physiotherapist's clinic but can instead undergo treatment from home, utilizing one or more sensors for guidance. This method is particularly significant given the escalating healthcare expenses associated with an aging population. Real-time consultations can be facilitated through video conferencing, whereas asynchronous interactions can involve guided exercise routines shared via digital platforms. Remote physiotherapy is beneficial for several reasons:

B. Enhancing Capabilities with Multiple Sensor Nodes

Integrating multiple sensor nodes, whether of the same type or varied, offers a broader spectrum of data collection and more robust rehabilitation support. A particularly impactful addition is the Surface Electromyography (sEMG) sensor module, which is instrumental in muscle activity monitoring. While the current design has been developed with this sensor type in mind, future iterations will integrate both IMU and sEMG sensors within a unified module. The synergy of these sensors allows for a more detailed and comprehensive assessment of body movement dynamics. However, this advancement also introduces new technological challenges,



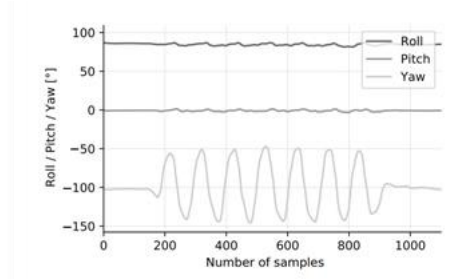


Fig. 15. Analysisof torso rotation. A periodic movement with an angular variation of \pm 50 in the yaw axis is detected, while the roll and pitch axes displayminorfluctuations.

digitallearnin@nvironments,tcontribut/09 to e-learnin@or physiotherapists/ostering improved skill acquisitionand training.

To summarize senso node enhances on vention al herapy by facilitating emote care, supporting ehabilitation and advancing reventive health strategies positioning a an essential of for contemporary hysiotherapy.

Fig 14: Visualization of the second exercise: lateral trunk rotation (Images sourced from Pocket Yoga (www.pocketyoga.com)). The arrow marks the sensor's placement.

- Patients can independently perform rehabilitation exercises with minimal supervision.
- Frequent travelers, such as professional athletes, can sustain their therapy under the same physiotherapist.
- It serves as a crucial alternative in scenarios where inperson visits are unfeasible, such as during public health crises like the COVID-19 pandemic.

The effectiveness of remote physiotherapy solutions has been rigorously investigated in [32]. Furthermore, this technology extends beyond treatment applications to include physiotherapy education. By integrating the proposed sensor into especially concerning synchronization at both intra- and intermodule levels to ensure accurate concurrent measurements. A synchronized clocking system can be

employed to align the IMU and sEMG sensors, mitigating clock drift discrepancies. To synchronize multiple sensor nodes, BLE beacon packets from a central node, such as the receiver, can be used, or a dedicated protocol can be designed [33]

For data transmission, a simple yet effective approach involves unidirectional beacon packets without requiring retransmission. While this method minimizes complexity, it does not guarantee that all packets reach their intended destination. A more robust alternative involves utilizing BLE retransmission capabilities to ensure successful packet delivery. Additionally, periodic synchronization beacon packets can be incorporated to maintain consistent timing across nodes. As functionality expands, both the electrical and mechanical complexities of the design will increase, necessitating innovative solutions to efficiently integrate

multiple features into a compact framework.

6. Conclusions and Future Prospects

Conclusions: This study introduces a wearable, wireless sensor node designed for motion tracking applications. The selection of components, software refinements, and an energyconscious design contribute to a device capable of continuous autonomous operation for up to 28 hours. An 'always-on' standby mode, eliminating the need for a physical button, extends battery longevity to approximately eight months, ensuring immediate usability upon activation. The paper provides a comprehensive explanation of the sensor node's calibration methodology, particularly emphasizing a photogrammetric validation process leveraging cost-effective and readily available tools. By incorporating an on-device sensor fusion algorithm based on the Madgwick filter, the system achieves an average static accuracy error of 3.28° and a drift of 2° over a 30-minute period. The finalized prototype weighs 38 grams and has a form factor of $\phi 6 \text{ cm} \times 1.5 \text{ cm}$. The results of this research demonstrate the feasibility of a cost-effective, user-friendly device that is beneficial for healthcare professionals and enables efficient patient monitoring. Furthermore, the system is wellsuited for real-time rehabilitation tracking and diverse motion analysis applications.

Future Prospects: Multiple pathways exist for improving and expanding the capabilities of the current sensor node. A key priority is conducting further validation by comparing the device's accuracy against specialized laboratorygrade equipment. The integration of additional sensors will be explored to enhance the depth of movement analysis. A newly developed sEMG sensor designed to measure muscle activity will be incorporated into the existing setup, allowing for simultaneous data collection. To achieve synchronized and precise measurements, mechanisms will be established to ensure alignment at both intra- and inter-node levels. A promising advancement involves implementing real-time calibration via artificial intelligence [34]. This feature could be realized using a power-efficient microcontroller, such as the nRF52832 by Nordic Semiconductor, which integrates an ARM Cortex M4 processor within the BLE module. Consolidating the Bluetooth stack and peripheral processing onto a single chip would eliminate the need for an additional Cortex M0+ microcontroller, reducing overall power consumption. Another promising improvement involves designing a custom PCB antenna to optimize wireless communication. Currently, the collected data is primarily visualized but not extensively processed. Incorporating advanced data analytics and machine learning techniques would enable the recognition and interpretation of intricate motion patterns. Additionally, a potential enhancement includes direct sensor-to-smartphone communication via a dedicated mobile application, eliminating the requirement for an external receiver.

7. References

- Porciuncula F, Roto AV, Kumar D, Davis I, Roy S, Walsh CJ, et al. Wearable movement sensors for rehabilitation: a focused review of technological and clinical advances. PM&R. 2018;10:S220-32. https://doi.org/10.1016/j.pmrj.2018.06.013
- 2. Eliko. Inertial motion capture system [Internet]. 2020 [cited 2020 Oct 27]. Available from: https://www.eliko.ee/shop/inertial-motioncapture-

- system/
- 3. Shimmer Sensing. IMU sensor development kit [Internet]. 2020 [cited 2020 Oct 27]. Available from: https://www.shimmersensing.com/products/shimmer3-development-kit
- 4. Cappelle J. Wireless motion sensor node [Internet]. 2020 [cited 2020 Nov 4]. Available from: https://github.com/DRAMCO/NOMADe-Wireless-Motion-Sensor-Node
- Brodie M, Walmsley A, Page W. The static accuracy and calibration of inertial measurement units for 3D orientation. Comput Methods Biomech Biomed Engin. 2008;11:641 https://doi.org/10.1020/10255840802078014
 - 8. https://doi.org/10.1080/10255840802078014
- 6. Vicon. Award winning motion capture systems [Internet]. 2020 [cited 2020 Sep 9]. Available from: https://www.vicon.com/
- Kadir K, Yusof ZM, Rasin MZM, Billah MM, Salikin Q. Wireless IMU: a wearable smart sensor for disability rehabilitation training. In: 2018 2nd International Conference on Smart Sensors and Application (ICSSA); 2018 Jul 24-26; Kuching, Malaysia. p. 53-7.
- 8. Petropoulos A, Sikeridis D, Antonakopoulos T. Wearable smart health advisors: an IMU-enabled posture monitor. IEEE Consum Electron Mag. 2020;9:20-7. https://doi.org/10.1109/MCE.2019.2953743
- TDK. ICM-20948 [Internet]. 2019 [cited 2019 Oct 26]. Available from: https://www.invensense.com/products/motion-tracking/9-axis/icm20948/
- Fei Y, Song Y, Xu L, Sun G. Micro-IMU based wireless body sensor network. In: 33rd Chinese Control Conference; 2014 Jul 28-30; Nanjing, China. p. 428-32.
- 11. Madgwick SOH, Harrison AJL, Vaidyanathan R. Estimation of IMU and MARG orientation using a gradient descent algorithm. In: 2011 IEEE International Conference on Rehabilitation Robotics; 2011 Jun 29-Jul 1; Zurich, Switzerland. p. 1-7.
- 12. Silicon Labs. EFM32 Happy Gecko family EFM32HG data sheet [Internet]. 2020 [cited 2020 Nov 6]. Available from: https://www.silabs.com/documents/public/data-sheets/efm32hg-datasheet.pdf
- 13. CH Robotics. Understanding Euler angles [Internet]. 2020 [cited 2020 May 6]. Available from: http://www.chrobotics.com/library/understanding -euler-angles
- 14. Tuupola M. How to calibrate a magnetometer? [Internet]. 2020 [cited 2020 Apr 10]. Available from: https://appelsiini.net/2018/calibrate-magnetometer/
- 15. Ergen S. ZigBee/IEEE 802.15.4 summary. Berkeley: UC Berkeley; 2004. Report No.: 10.
- Ab Rahman AB. Comparison of Internet of Things (IoT) data link protocols [Internet]. 2020 [cited 2020 Nov 7]. Available
 - from: https://www.semanticscholar.org/paper/Comparis on-of-Internet-of-Things-(-IoT-)-Data-LinkRahman/1cf94e2ebb27aaecdae3742e444ca9e87314216
- Danbatta SJ, Varol A. Comparison of Zigbee, ZWave, Wi-Fi, and Bluetooth wireless technologies used in home automation. In: 2019 7th International Symposium on Digital Forensics and Security (ISDFS); 2019 Jun 10-12; Barcelos, Portugal. p. 1-5.

- Würth Elektronik. Proteus-II Bluetooth Smart 5.0 module (AMB2623) [Internet]. 2019 [cited 2019 Oct 26]. Available from: https://katalog.we-online.de/en/wco/WIRL_BTLE_5
- 19. Keil. Cx51 user's guide: floating-point numbers [Internet]. 2020 [cited 2020 Mar 18]. Available from: http://www.keil.com/support/man/docs/c51/c51_ap_floatingpt.htm
- STMicroelectronics. NUCLEO-L4R5ZI STM32 Nucleo-144 development board with STM32L4R5ZI MCU [Internet]. 2020 [cited 2020 Mar 17]. Available from: https://www.st.com/en/evaluation-tools/nucleo-14r5zi.html
- 21. Simply Embedded. UART receive buffering [Internet]. 2020 [cited 2020 Mar 17]. Available from: http://www.simplyembedded.org/tutorials/interrupt-free-ring-buffer/
- 22. Semtech. Semtech releases next-generation LinkCharge®LP (low power) wireless charging platform [Internet]. 2020 [cited 2020 Nov 6]. Available from: https://www.semtech.com/company/press/semtech-releases-next-generation-linkcharge-lp-lowpower-wireless-charging-platform
- 23. Texas Instruments. BQ5105xB high-efficiency Qi v1.2-compliant wireless power receiver and battery charger [Internet]. 2020 [cited 2020 Nov 6]. Available from: https://www.ti.com/lit/ds/symlink/bq51051b.pdf
- 24. ValueWalk. Galaxy S10 reverse wireless charging feature: how to use it [Internet]. 2019 [cited 2020 Nov 6]. Available from: https://www.valuewalk.com/2019/03/galaxy-s10-reverse-wireless-charging/
- 25. Würth Elektronik. WE-WPCC wireless power charging receiver coil 760308101214 [Internet]. 2020 [cited 2020 Nov 6]. Available from: https://www.we-online.com/catalog/datasheet/760308101214.pdf
- 26. Puers R. Inductive powering: basic theory and application to biomedical systems. 1st ed. Dordrecht: Springer; 2009.
- 27. Image Labs. Computer controlled pan-tilt unit model PTU-D46 [Internet]. 2020 [cited 2020 Nov 6]. Available from: www.imagelabs.com/wp-content/uploads/2011/01/Specs-PTU-D46.pdf
- 28. Madgwick SOH. An efficient orientation filter for inertial and inertial/magnetic sensor arrays. Bristol: x-io Technologies, University of Bristol; 2010. Report No.: 25. p. 113-8.
- 29. Shi J, Tomasi C. Good features to track. In: IEEE Conference on Computer Vision and Pattern Recognition; 1994 Jun 21-23; Seattle, WA. p. 593-600.
- Isard M, Blake A. CONDENSATION conditional density propagation for visual tracking. Int J Comput Vis. 1998;29:5-28. https://doi.org/10.1023/A:1008078328650
- 31. de Kok J, Vroonhof P, Snijders J, Roullis G, Clarke K, Peereboom K, *et al.* Work-related musculoskeletal disorders: prevalence, costs and demographics in the EU. Bilbao: European Agency for Safety and Health at Work; 2019.
- 32. Dierick F, Buisseret F, Brismee JM, Fourré A, Hage R, Leteneur S, *et al.* Opinion on the effectiveness of physiotherapy management of neuro-musculo-skeletal disorders by telerehabilitation [Internet]. 2020 [cited 2020 Oct 27]. Available

- from: https://www.ifompt.org/site/ifompt/Telerehab_E N.pdf
- 33. Coviello G, Avitabile G, Florio A. A synchronized multi-unit wireless platform for long-term activity monitoring. Electronics. 2020;9:1118. https://doi.org/10.3390/electronics907111
- 34. Claesson E, Marklund S. Calibration of IMUs using neural networks and adaptive techniques targeting a self-calibrated IMU [Master's thesis]. Gothenburg: Chalmers University of Technology; 2019.